ACS OMEGA

Article

http://pubs.acs.org/journal/acsodf

Coupling of Crumpled-Type Novel MoS_2 with CeO_2 Nanoparticles: A Noble-Metal-Free p−n Heterojunction Composite for Visible Light Photocatalytic H_2 Production

Gayatri Swain, Sabiha Sultana, Brundabana Naik, and Kulamani Parida*

Centre for Nano Science and Nanotechnology, Siksha O Anusnadhan University, Bhubaneswar 751030, Odisha, India

Supporting Information

ABSTRACT: In terms of solar hydrogen production, semiconductor-based photocatalysts via p−n heterojunctions play a key role in enhancing future hydrogen reservoir. The present work focuses on the successful synthesis and characterization of a novel p-MoS_2/n-CeO_2 heterojunction photocatalyst for excellent performance toward solar hydrogen production. The synthesis involves a simple in situ hydrothermal process by varying the wt % of MoS_2. The various characterization techniques support the uniform distribution of CeO_2 on the surface of crumpled MoS_2 nanosheets, and the formation of p−n heterojunction is further confirmed by transmission electron microscopy and Mott−Schottky analysis. Throughout the experiment, it is demonstrated that 2 wt % MoS_2 in the MoS_2/CeO_2 heterojunction photocatalyst exhibits the highest rate of hydrogen evolution with a photocurrent density of 721 μA cm^{-2}. The enhanced photocatalytic activity is ascribed to the formation of the p−n heterojunction that provides an internal electric field to facilitate the photogenerated charge separation and transfer.

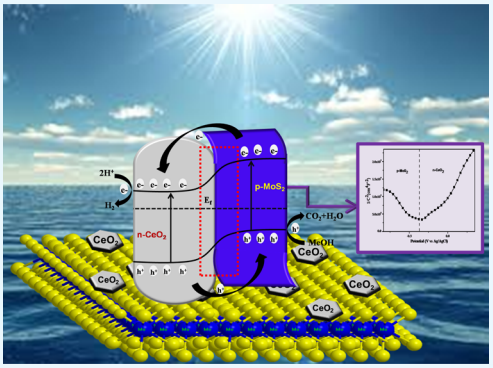

INTRODUCTION

Development of a visible-light-driven photocatalyst to produce hydrogen by water splitting using solar energy is an attractive environmentally friendly method, which offers a way for capturing available solar energy and converting it into hydrogen.[1] Although many photocatalysts capable of splitting water have been developed, most of them are oxides.[1c,2] CeO_2 is one of the widely accepted metal oxide photocatalysts, which have been studied over more than decades. Its high chemical stability, nontoxicity, and low cost make it a promising candidate like TiO_2 and ZnO.[3] However, the application of CeO_2 as a photocatalyst is hindered by some of the drawbacks, that is, wide band gap, narrow light absorption ability, and high recombination rate.[4] Thus, more studies have been performed demonstrating improvement in the photocatalytic activity by strategies such as band gap engineering, doping, physical property tuning, and making suitable active site availability. But one of the most effective strategies is the development of a heterostructure instead of designing impurity doping. Combining a wide-band-gap material with a smaller-band-gap semiconductor such as metal dichalcogenides harvests a broader-spectrum absorption of solar energy and promotes charge separation.[5,3c]

Recent studies introduced functional two-dimensional (2D) layered-structured graphene analogous materials, such as MoS_2, as a photocatalyst, which have attracted considerable attention in the fields of energy technology, photonics, nanoelectronics, and materials science by virtue of their unique material properties, unique chemical and electronic properties, efficient cocatalytic supports, suitable band gaps, and diverse applications.[6] MoS_2 is a layered-structured material designed from Mo atoms sandwiched between two layers of hexagonally close-packed S atoms with a stoichiometry of MoS_2. Because of a weak van der Waals gap between layers, it can be exfoliated into single- or few-layered nanosheet-like graphene, which has various applications in Li-ion batteries, sensing, photo-transistors, and photocatalytic hydrogen production.[7] More importantly, MoS_2 is considered as a better substitute for noble metals (such as Pt, Rh, Ru, Pd) as well as a low-cost cocatalyst for both photocatalytic and electrocatalytic H_2 evolution due to the existence of highly exposed edges derived from the MoS_2 crystal layers.[8] Although it possesses many fascinating properties, alone it is inactive toward the solar-light-driven hydrogen evolution reaction.[8e] Thus, many studies have been conducted by taking MoS_2 either as a cocatalyst or as a component in heterojunction-based materials.[9] But heterojunction photocatalyst materials are considered to be the most promising candidates because they provide a potential driving force, which facilitates the separation of photoexcited charge carriers, dominates the transfer direction, increases the contact interface, and accelerates the rate of charge transfer within the heterojunction compartment.[10,2f,3c] The construction of heterojunctions make the hydrogen evolution mechanism easier by developing the typical type-II heterostructure mode because of

Received: April 21, 2017
Accepted: June 27, 2017
Published: July 19, 2017

DOI: 10.1021/acsomega.7b00492
ACS Omega 2017, 2, 3745−3753

the staggered band gap structure between the two semiconductors followed by enhancing the overall energy conversion efficiency.[2e,3b] The p-type MoS_2 has been reported in many literature reports and shows better results toward both photocatalytic and photoelectrocatalytic H_2 evolution. The p-type behavior of MoS_2 is attributed to its good electronic properties; narrow band gap, which broadens the visible light response; high thermal stability; large specific surface area; and electrostatic integrity. Hence, it results in good photogenerated charge transfer through the intimate contact of the heterojunction, increasing the photocatalytic H_2 evolution activity. Yuan et al. developed a 2D−2D nanojunction between MoS_2 and TiO_2 and tested the photocatalytic water reduction reaction.[9a] A number of studies have been reported for enhancing the photocatalytic performance due to heterojunctions such as *n*-$BiVO_4$-MoS_2,[11] MoS_2-MoO_3/CdS,[12] MoS_2/CdS,[13] and MoS_2/N-RGO/CdS.[14]

Among different nanocomposite heterojunctions, the p−n heterojunction between two semiconductors has been reported as the most challenging and effective photocatalytic material because it generates a space charge region, which is due to the depletion of electrons from the n-type semiconductor and holes from the p-type semiconductor near that region.[13] The present photocatalytic scheme suggests a p−n heterojunction nanocomposite photocatalyst considering MoS_2 as a p-type semiconductor and CeO_2 as an n-type semiconductor, and this will give an intimate contact area, which may promote the photogenerated charge carriers at the interface of the MoS_2/CeO_2 nanocomposite. Gong et al. have reported a MoS_2/CeO_2 hybrid core−shell nanostructure, which shows enhanced catalytic activity in ammonia decomposition toward H_2 production.[15] Again, Li and his co-workers constructed a CeO_2@MoS_2 core−shell nanocomposite, which plays a better role in symmetric supercapacitors.[16] In addition the other work reported by Li et al. in which a ternary attapulgite−CeO_2/MoS_2 nanocomposite was designed, which activity is fabricated by degrading dibenzothiophene in gasoline under visible light irradiation.[17] From the foregoing discussion, it is concluded that there is no such reported H_2 evolution via heterojunction photocatalysts for the MoS_2/CeO_2 nanocomposite.

In this work, we have successfully coupled n-type CeO_2 with layered p-type MoS_2 in a 2D heterojunction fashion through a facile hydrothermal method. In addition, the coupled heterojunction exhibits an intimate junction between n-CeO_2 and p-MoS_2, which we have confirmed from transmission electron microscopy (TEM) and Mott−Schottky plots. The improved charge transfer and separation across the p−n junction is mainly responsible for the enhanced photocatalytic water-splitting activity under simulated solar irradiation.

RESULTS AND DISCUSSION

The powder X-ray diffraction (XRD) characterization of the as-synthesized semiconductor photocatalyst was employed to certify the phase, crystal structure, composition, and purity. The XRD patterns of pristine MoS_2, CeO_2, and the MoS_2/CeO_2 nanocomposite are shown in Figure 1. It was detected that the peaks at 2θ of 28.49, 33.01, 47.42, and 56.25 represent the planes (111), (200), (220), and (311), respectively, with the corresponding *d*-spacing values of 3.12, 2.71, 1.92, and 1.63 Å, which revealed the cubic structure of CeO_2 (which can be correlated to TEM images). This is in a good agreement with the JCPDS file no. 34-0394.[18] The characteristic diffraction peaks shown by MoS_2 indexed to the (002), (004), (100),

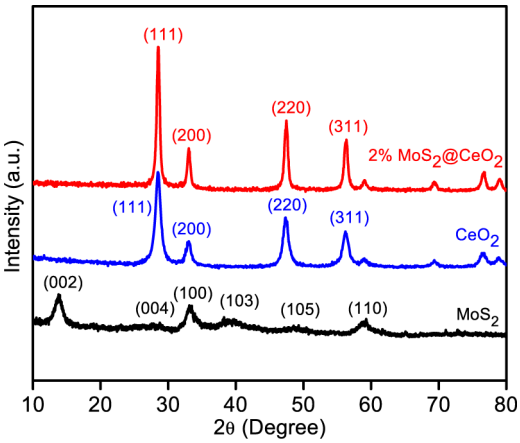

Figure 1. XRD spectra of MoS_2, CeO_2, and the 2% MoS_2/CeO_2 composite.

(103), (105), and (110) planes are of 2H hexagonal MoS_2, which satisfies the JCPDS no. 37-1492.[19] There was no other prominent peak present which implied good crystallinity and high purity of the sample. Interestingly, it was unambiguous that the intensity of typical peaks of CeO_2 in the MoS_2/CeO_2 nanocomposite increased significantly and became slightly sharp after loading the various weight percentages of MoS_2. This could be due to increase in the crystallinity of CeO_2 nanoparticles with the increase in the loading amount of MoS_2. However, no characteristic patterns of MoS_2 were examined in the XRD spectra of as-synthesized MoS_2/CeO_2 nanocomposites, probably owing to the low MoS_2 content and fine dispersion of MoS_2 on the surface of CeO_2 nanoparticles in the MoS_2/CeO_2 photocatalyst. It was also noted that the peaks at 2θ of 28.49, 33.01, and 47.42 assigned to the (111), (200), and (220) planes slightly shifted toward a lower Bragg's 2θ angle after introduction of MoS_2, which concluded the synergistic interaction between MoS_2 with CeO_2.[20]

TEM measurements were further performed to analyze the morphological characteristics of the sample. The TEM image of CeO_2 from Figure 2a clearly displayed the formation of nanoparticles with an average lateral particle size of 25−30 nm. The inset of Figure 2a illustrates the well-defined fringes with lattice spacing d = 0.31 nm corresponding to the (111) plane of cubic CeO_2.[15] The TEM image of MoS_2 indicating the exfoliated nanosheets, which are crumpled together, is shown in Figure 2b.[19] Figure 2c depicts the distribution of CeO_2 nanoparticles (yellow framed portion) on crumpled MoS_2 nanosheets. However, hexagonal CeO_2 nanoparticles were not clearly visible due to wrapping of MoS_2 nanosheets around these nanoparticles. In the high-resolution TEM image, the presence of both CeO_2 and MoS_2 fringes indicated the effective formation of heterojunction. A clear lattice fringe of approximately 0.62 nm is ascribed to the (002) plane of MoS_2, and another set of fringes with an interplanar distance of about 0.31 nm corresponds to the (111) lattice plane of CeO_2.[7a] The energy-dispersive X-ray (EDX) pattern of the as-synthesized composite photocatalyst is shown in Figure S1 in the Supporting Information, which depicted the successful intimate interaction of CeO_2 on the sheet of crumpled MoS_2 that facilitates the separation of photogenerated charge carriers. Furthermore, the corresponding EDX pattern showed the presence of low concentration of MoS_2 because it is about only 2%.

DOI: 10.1021/acsomega.7b00492
ACS Omega 2017, 2, 3745−3753

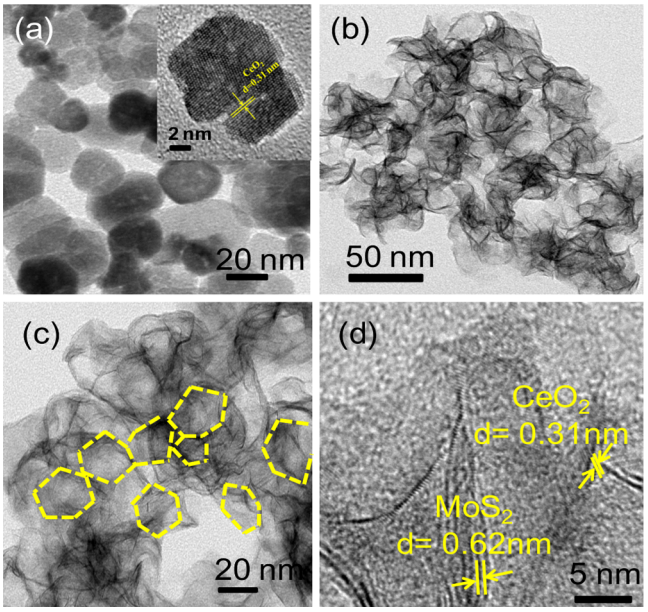

Figure 2. TEM images of (a) CeO_2 nanoparticles (inset figure shows the fringe pattern of pure CeO_2), (b) crumpled MoS_2 nanosheet, (c) 2% MoS_2/CeO_2 nanocomposite, and (d) fringe pattern of the MoS_2/CeO_2 nanocomposite.

X-ray photoelectron spectroscopy (XPS) was used to explore the surface chemical environmental composition as well as the valence state of the various elements present in the MoS_2/CeO_2 nanocomposite sample. Figure 3 shows the core-level XPS peaks of the 2% MoS_2/CeO_2 nanocomposite. All of the binding energies were measured by taking the C 1s peak of surface adventitious carbon at 284.9 eV as the reference body in the instrument whose presence was confirmed in the survey spectra of XPS.[11] The binding energy measurement evaluates the bonding information and elementary composition of samples. The XPS survey spectrum shown in Figure 3a indicated the existence of Mo, S, Ce, and O, which are the constituent elements of the MoS_2/CeO_2 nanocomposite material. XPS scan spectra of individual components present in the as-obtained nanocomposite photocatalyst are also mentioned in Figure 3. The indication of reduction of Mo^{6+} to Mo^{4+} in the formation of MoS_2 from the Mo precursor was confirmed from the XPS spectra of Mo 3d (Figure 3b) for which the doublet binding energies were obtained at 233.0 and 229.9 eV for $3d_{3/2}$ and $3d_{5/2}$ in the 2% MoS_2/CeO_2 sample, respectively.[6c,21] The sulfur in MoS_2 is present as sulfide S^{2-} with 1.69% atomic concentration. From Figure 3c, it could be obvious that after deconvolution Ce reflects two sets of core-level XPS spectra, one type for $3d_{5/2}$ (880−900 eV) and another set for $3d_{3/2}$ (900−920 eV). As demonstrated in Figure 3c, multiple splitting of both the spin states, that is, $3d_{5/2}$ and $3d_{3/2}$, of Ce belongs to the mixed valence state, such as the Ce^{3+} and Ce^{4+} oxidation states, owing to its nonstochiometric nature. The multiple d-splitting displays XPS peaks at 916.4 and 898.04 eV for Ce^{4+} $3d_{3/2}$ and $3d_{5/2}$, respectively, corresponding to the two main characteristic XPS peaks of Ce, and the peaks located at 900.5 and 881.9 eV belong to Ce^{3+} $3d_{3/2}$ and $3d_{5/2}$,

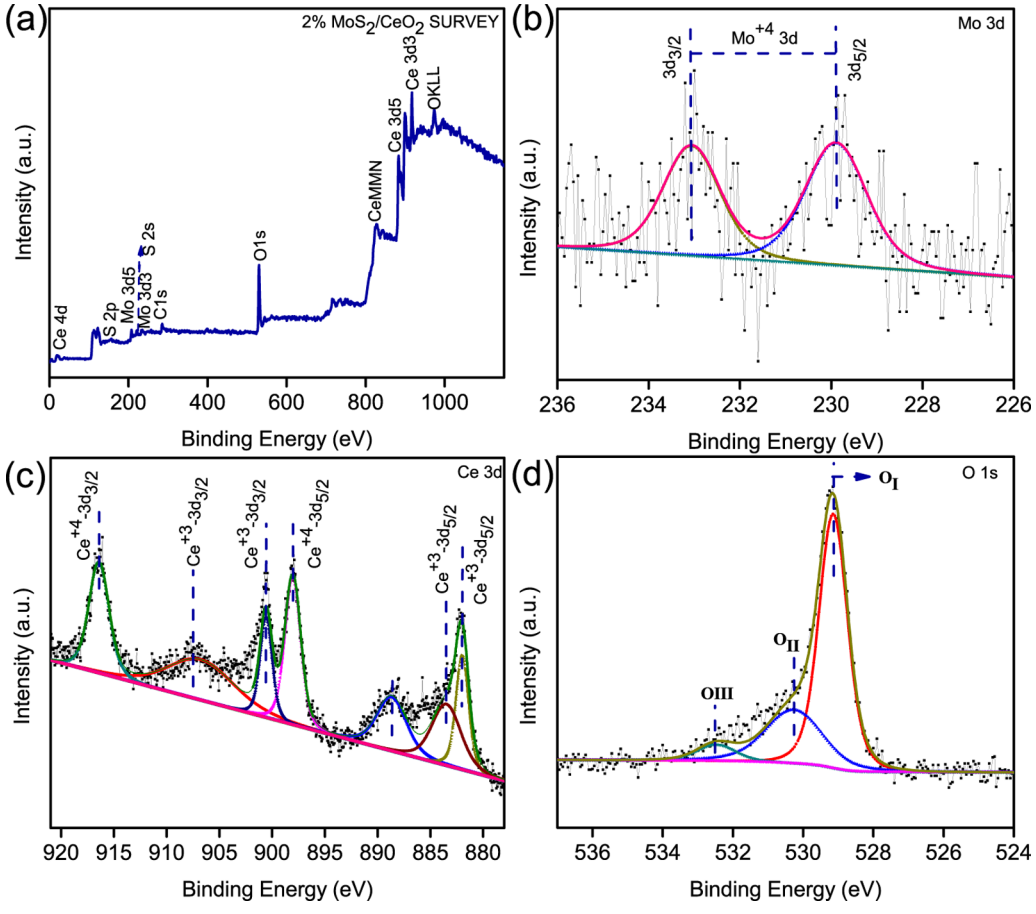

Figure 3. XPS spectra of the 2% MoS_2/CeO_2 nanocomposite: survey spectrum (a), Mo 3d (b), Ce 3d (c), and O 1s (d).

DOI: 10.1021/acsomega.7b00492
ACS Omega 2017, 2, 3745−3753

respectively. In addition, other three satellite peaks were observed for Ce^{3+} $3d_{3/2}$ at 907.1 and for Ce^{3+} $3d_{5/2}$ at 888.7 and 885.1 eV.[22]

The XPS peaks of the O 1s in nanocomposite demonstrated in Figure 2d contain three core-level types of oxygen peaks. The lower binding energy at 529.1 eV corresponds to the lattice oxygen (O_I) and the higher binding energy at 532.5 eV indicates the core-level oxygen (O_{III}). It suggests the chemisorbed oxygen forming the O−H radical after dissociation from the superoxide ion. In addition to the above two oxygen peaks, there is another core-level O 1s peak (O_{II}) obtained at the binding energy of 530.24 eV, which describes the presence of oxygen vacancy in the lattice site of CeO_2 nanoparticles.[22a]

The optical absorption properties and the electronic structural features of the as-prepared neat and composite samples were studied by recording ultraviolet−visible (UV−vis) diffuse reflectance spectra. The UV−vis diffuse reflectance spectra of the neat and composite samples with different amounts of MoS_2 are shown in Figure 4. Pristine CeO_2 showed a sharp fundamental absorption peak at about 430 nm, and it was noticed that the intensity of the absorption peaks of composite samples rises as more amount of MoS_2 was exposed to the surface of CeO_2. It may be due to the black color of MoS_2. As the loading content of MoS_2 in the MoS_2/CeO_2 nanocomposite increases, there was a notable change in the absorbance intensity edge of the composites, which was in good agreement with color changes from light yellow to light brown.[6b] In addition, the band edge potential of the samples was calculated by the Schuster−Kubelka−Munk equation and all composites show a direct band gap similar to that of neat CeO_2.[23] The band gap energy of neat CeO_2 and MoS_2 corresponding to the energy at about 2.97 (absorption at around 430 nm) and 1.89 eV, respectively, is shown in Figure S2a,b. Thus, the introduction of MoS_2 into the composite may facilitate the improvement of the charge separation and show full visible spectrum absorption.

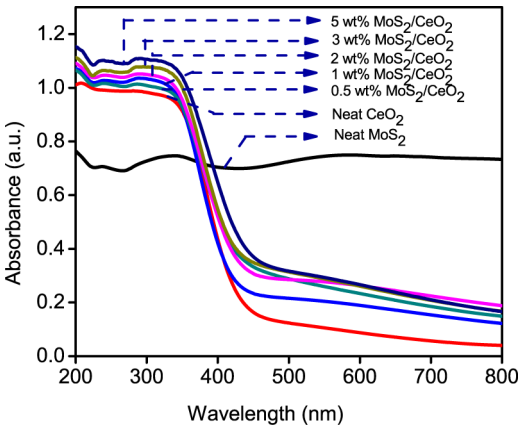

Figure 4. UV−vis diffuse reflectance spectra of neat CeO_2, neat MoS_2, and MoS_2/CeO_2 nanocomposite.

Generally, the photocatalytic activity of photocatalysts is related to their band structure. Thus, the corresponding band edge positions of both CeO_2 and MoS_2 were estimated from the following equation.

$$E_{VB} = X - E^e + 0.5E_g$$

Herein, X is the geometric mean of the electronegativity of the constituent atoms present in a semiconductor, E^e is the energy of free electrons on the hydrogen scale (~4.5 eV), and E_g is the band gap energy of the semiconductor.[24] The X values for CeO_2 and MoS_2 are calculated to be 5.578 and 5.32 eV, respectively. From this equation, E_{VB} of CeO_2 and MoS_2 were calculated to be 2.56 and 1.76 eV, respectively, and the corresponding E_{CB} positions were calculated to be −0.41 for CeO_2 and −0.13 for MoS_2.

PHOTOCATALYTIC ACTIVITY VIA H_2 EVOLUTION MEASUREMENT AND MECHANISM

The photocatalytic activities of CeO_2 and the MoS_2/CeO_2 nanocomposite were performed for hydrogen evolution through the water-splitting reaction, in the presence of methanol as the sacrificial hole scavenger at ambient temperature and atmospheric pressure. There is no evolution of H_2 gas in the absence of light as well as catalyst. Figure 5a shows the hydrogen evolution rate of different wt % loadings of MoS_2 onto CeO_2. The pure CeO_2 sample shows an extremely poor photocatalytic H_2 evolution (proceeding without the use of a UV cutoff filter) rate of around 8.93 μmol h^{-1} due to the large band gap of about 2.97 eV (restricted only to the UV range) and faster recombination of the photogenerated charge carrier.[4]

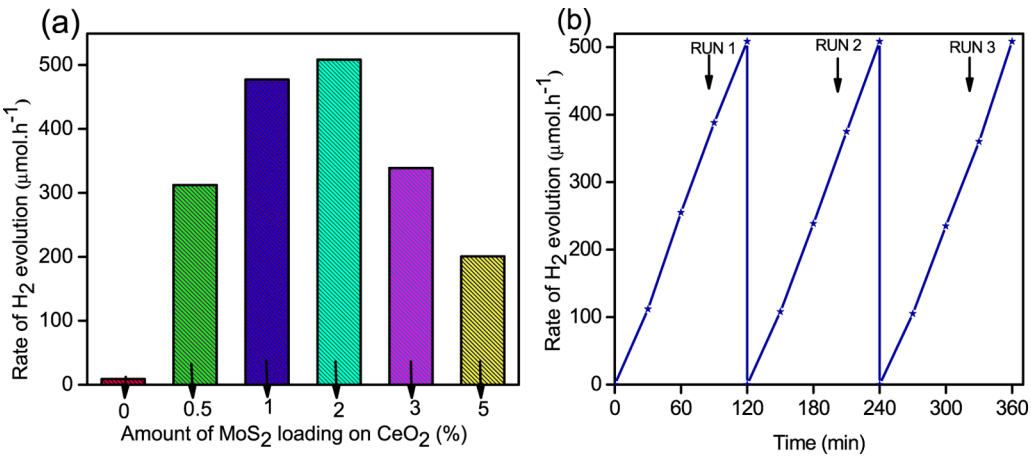

Figure 5. Rate of H_2 production of neat CeO_2 and the MoS_2/CeO_2 nanocomposite with various amounts of MoS_2 loading (a) and the cycling test for H_2 evolution of the MoS_2/CeO_2 nanocomposite with 2 wt % MoS_2 (b).

DOI: 10.1021/acsomega.7b00492
ACS Omega 2017, 2, 3745−3753

Again, pure MoS_2 itself is very much inactive toward solar-light-driven hydrogen evolution, which may be due to the low carrier density. Figure 5a reflects the considerable increase in the H_2 evolution rate of the MoS_2/CeO_2 composite than that of neat CeO_2. This study displayed the effect of loading and also intimate heterojunction between CeO_2 and MoS_2, which facilitates high separation efficiency and effective channelization of photogenerated charge carriers. As a consequence, the formation of the MoS_2/CeO_2 grain boundary and heterojunction can also be seen in the TEM images shown in Figure 2d and the heterojunction facilitates the electron transfer between the two compartments to improve the photocatalytic H_2 evolution activity.[10a] H_2 evolution trend increased remarkably up to 2% of MoS_2 loading and then decreased gradually afterward for 3 and 5%, which is in accordance with the photoluminescence (PL) study. Moreover, CeO_2 shows H_2 evolution rates of 312.2 and 477.22 μmol h^{-1} when the loading amounts of MoS_2 are 0.5 and 1%, respectively. In the present study, 2 wt % of MoS_2 shows the highest H_2 evolution rate (508.44 μmol h^{-1}), which is 57 times better than that of neat CeO_2. Afterward, the H_2 evolution rate decreased when the loading amount of MoS_2 exceeded 2 wt %, and this phenomenon can be ascribed to the intensive absorption of light by the large black color MoS_2, which shields the active sites on the surface of the MoS_2/CeO_2 nanocomposite.[25] This is in good agreement with the absorption spectra shown in Figure 4. The hydrogen evolution values shown by 3 and 5 wt % MoS_2/CeO_2 nanocomposite are 338.96 and 223.01 μmol h^{-1}, respectively, which are quite smaller than the other loading percentages of MoS_2. However, about ±2% error has been found throughout the experiments. In addition to the photocatalytic activity of the sample, it is necessary to explore the stability of the photocatalyst in the practical experiment. To investigate the stability of the photocatalyst, a recycle study of hydrogen evolution was performed under the same reaction conditions. Figure 5b shows the recyclability of hydrogen evolution of the best performing 2 wt % MoS_2/CeO_2 photocatalyst of three times with a time induction period of 2 h. Even after 6 h of the reaction in three repeated cycles, there is no decrease of H_2 evolution, suggesting the photostability of the catalyst.

The PL and Nyquist (electrochemical impedance spectra (EIS)) spectra of the as-prepared MoS_2, CeO_2, and MoS_2/CeO_2 nanocomposite samples were recorded to investigate the enhanced photocatalytic activity, which may be due to the synergistic effect of few-layered MoS_2 loading on the MoS_2/CeO_2 nanocomposite.

PL spectroscopy was mainly carried out to know the recombination rate of photogenerated excitons, such as electrons and holes. The sharp intensity of PL spectra depends upon the rate of recombination of photogenerated excitons. It has been observed that the higher the recombination rate of electron/hole pairs the higher the PL emission. From PL spectra, we can also extract the idea about the generation, migration, and separation efficiency of photoexcited charge carriers in a number of semiconductor photocatalysts.[26] Figure 6 shows the PL spectra of the pure and composite samples under the same conditions with an excitation wavelength of 340 nm. A strong blue emission peak is observed at 427.5 nm, and the existence of this peak is due to the formation of an extra surface defect energy level between the O 2p and Ce 4f band levels. It is observed that the sharpness of the peak falls down as the amount of the loading percentage of MoS_2 increases,

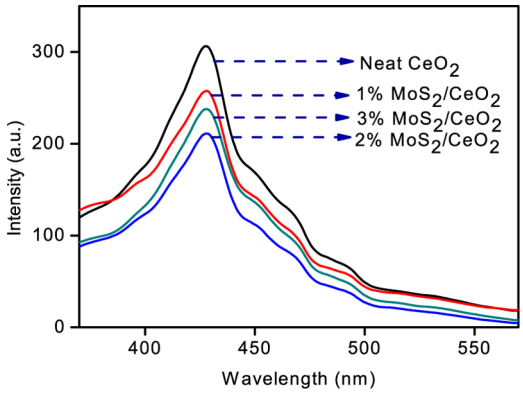

Figure 6. PL emission spectra of neat CeO_2 and various nanocomposites.

competing with the neat CeO_2. This trend is followed up to 2 wt % MoS_2 on CeO_2; afterward, there is an increase in the peak intensity with an increase in the loading percentage of MoS_2, that is, for 3 and 5 wt %, which may be due to the fast recombination of photogenerated electrons and holes. Zhao et al. have observed similar types of PL behavior for n-$BiVO_4$@P-MoS_2 toward photocatalytic reduction and oxidation.[10b] The suppression of PL peak in the 2 wt % MoS_2/CeO_2 photocatalyst may be due to the efficient interfacial electron transfer between the excited CeO_2 energy level and MoS_2. The 2 wt % MoS_2/CeO_2 composite showed the highest photocatalytic activity, which is in good agreement with the above PL observation. The above study results in a better charge separation in the MoS_2/CeO_2 nanocomposite, leaving more redox excitons, which enhanced photocatalytic hydrogen evolution in nanocomposite samples.

Figure 7a shows the Nyquist (EIS) plots of CeO_2 and MoS_2/CeO_2 at zero biasing. Generally the plots are composed of a line in the lower-frequency region and a semicircle in a high-frequency region. The smaller the semicircle diameter, the smaller the interfacial charge transfer resistance and thus the higher the charge transfer and separation efficiency and the higher the electrical conductivity of the materials. In this case, a reduction in the semicircle diameter depicts that the resistance offered for the charge transportation is decreased significantly by adding MoS_2 in CeO_2. Meanwhile, the straight-line portion of the plot is smaller for the composite than that for CeO_2, which indicates the short diffusion path length of ions in the electrolyte.[6a,27]

In general, MoS_2 does not give any trace amount of H_2 in powdered photocatalysis, and the high-band-gap CeO_2 gives a very low amount of H_2 gas from photocatalytic water splitting. But the combination of MoS_2 and CeO_2 gave a much higher value of hydrogen evolution than that of their individual component. This enhanced photocatalytic performance may be due to the formation of an effective junction, which efficiently favors electron transfer as well as separation across the interface of MoS_2/CeO_2, which has good agreement with the Nyquist and PL plots. To gain more insight into the mechanism, linear sweep voltammetry (LSV) plots were acquired for CeO_2 and 2 wt % MoS_2/CeO_2 in 0.1 M NaOH with light irradiation (Figure 7b). The plot reflects the cathodic photocurrent for the reduction of protons at the electrode surface, and it was found that the onset potential for the CeO_2 electrode was −0.45 V (vs Ag/AgCl), whereas the onset potential was decreased to −0.20 V (vs Ag/AgCl) for the 2 wt % MoS_2/CeO_2 electrode. The

DOI: 10.1021/acsomega.7b00492
ACS Omega 2017, 2, 3745−3753

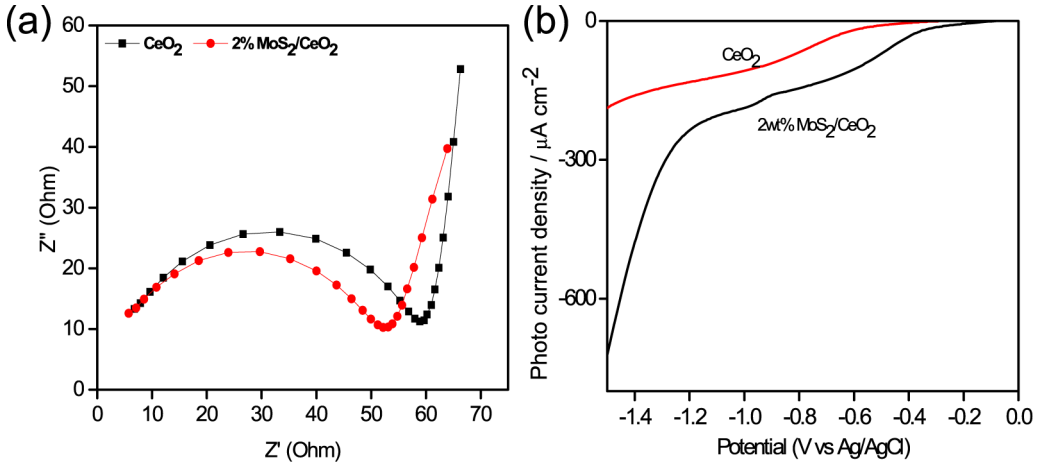

Figure 7. EIS of CeO_2 and the 2% MoS_2/CeO_2 nanocomposite (a) and the polarization curve for neat CeO_2 and the 2% MoS_2/CeO_2 nanocomposite (b).

significant reduction in the onset potential for H^+ reduction and high photocurrent density of 721 μA cm^{-2} of the 2 wt % MoS_2/CeO_2 composite compared to that of CeO_2 can be attributed to the formation of an effective junction between the two materials, thus improving the electron transfer rate and facilitating charge separation.[28]

On the basis of all of the above observations, we illustrate the mechanistic pathway for the MoS_2/CeO_2 heterostructure, as shown in Figure 9. The n-type conductivity of CeO_2 and p-type conductivity behavior of MoS_2 were investigated from the Mott–Schottky plot, as shown in Figure S3a,b. From the figure, the slope for CeO_2 is found to be low, whereas the slope for MoS_2 is very high, which implies the low carrier density and poor conductivity of MoS_2,[13] and they have shown type-I heterojunction before contact. The Fermi level of CeO_2 is higher than that of MoS_2, as shown in Figure 9a. But when a contact is formed between CeO_2 and MoS_2, the electrons from CeO_2 with a higher Fermi level will migrate toward the lower Fermi level of MoS_2 until both the Fermi levels come into symmetry, as shown in Figure 9b. After equilibrium is attained between the Fermi levels of both p-MoS_2 and n-CeO_2, the internal electric field in the p–n junction region leads to a potential difference at the interfaces of MoS_2/CeO_2, with its field direction from n-type CeO_2 to p-type MoS_2.[2929] To validate this fact, we have acquired Mott–Schottky plots, which show the presence of both positive (p-MoS_2) and negative (n-CeO_2) slopes, attributed to the presence of p–n junctions,[12] as shown in Figure 8.

Under solar light irradiation, both CeO_2 and MoS_2 will excite and produce photogenerated electrons and holes in their corresponding conduction band (CB) and valence band (VB), respectively. After the formation of p–n junction, the band bending was observed and the CB position of MoS_2 shifted upward than that of CeO_2. The band bending was because of the differences in the work functions of CeO_2 and MoS_2, and it is mainly due to MoS_2 because its carrier density is very low as compared to that of CeO_2.[13] Thus, the photogenerated electrons from MoS_2 are transferred to the lower-positioned CB of CeO_2 and simultaneously holes from the VB of CeO_2 are migrated toward the higher-potential VB of MoS_2, as shown in Figure 9c. Thus, the photogenerated electrons and holes remain separated due to the existence of an internal electric field formed by the p–n junction. Therefore, the highly reducible electrons are transferred to the surface of CeO_2 where

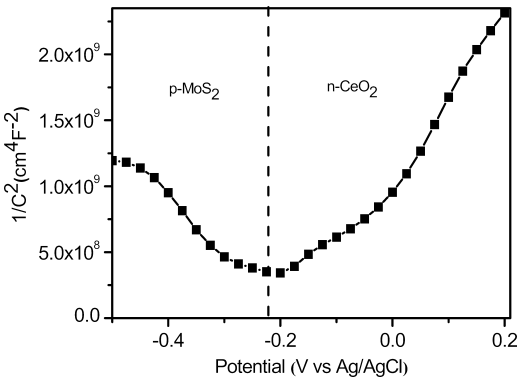

Figure 8. Mott–Schottky plot of the 2% MoS_2/CeO_2 nanocomposite.

they reduced the adsorbed water to H_2; similarly, holes are quenched by methanol on the surface of MoS_2. This phenomenon leads to an enhanced separation of photoexcitons, which suppresses the recombination process and enhances the overall photoactivity.

CONCLUSIONS

In summary, a facile in situ hydrothermal technique was proposed to successfully synthesize the novel MoS_2/CeO_2 heterojunction nanocomposite for photocatalytic H_2 production under visible light irradiation. The various characterizations firmly supported the formation of the MoS_2/CeO_2 nanocomposite, in which CeO_2 nanoparticles were uniformly decorated on the surface of MoS_2 sheet. Optimizing the overall experiment, it was demonstrated that the 2 wt % MoS_2/CeO_2 heterojunction nanocomposite showed the highest rate of H_2 evolution of 508.44 μmol h^{-1}, which is about 57 times more than that of neat CeO_2. For the better enhancement of the hydrogen evolution rate, the band alignment parameters play a key role via the p–n heterojunction, which provides a large intimate and contact interface between MoS_2 and CeO_2. Moreover, the designed p–n junction mechanism facilitates easier separation and transfer of photoinduced charge carriers such as electrons and holes. In the present work, the MoS_2/CeO_2 heterojunction-type nanocomposite photocatalyst toward solar-driven H_2 evolution has been constructed for the first time, which provides a simple, cost-effective, ecofriendly technique and good interface engineering for developing highly

DOI: 10.1021/acsomega.7b00492
ACS Omega 2017, 2, 3745–3753

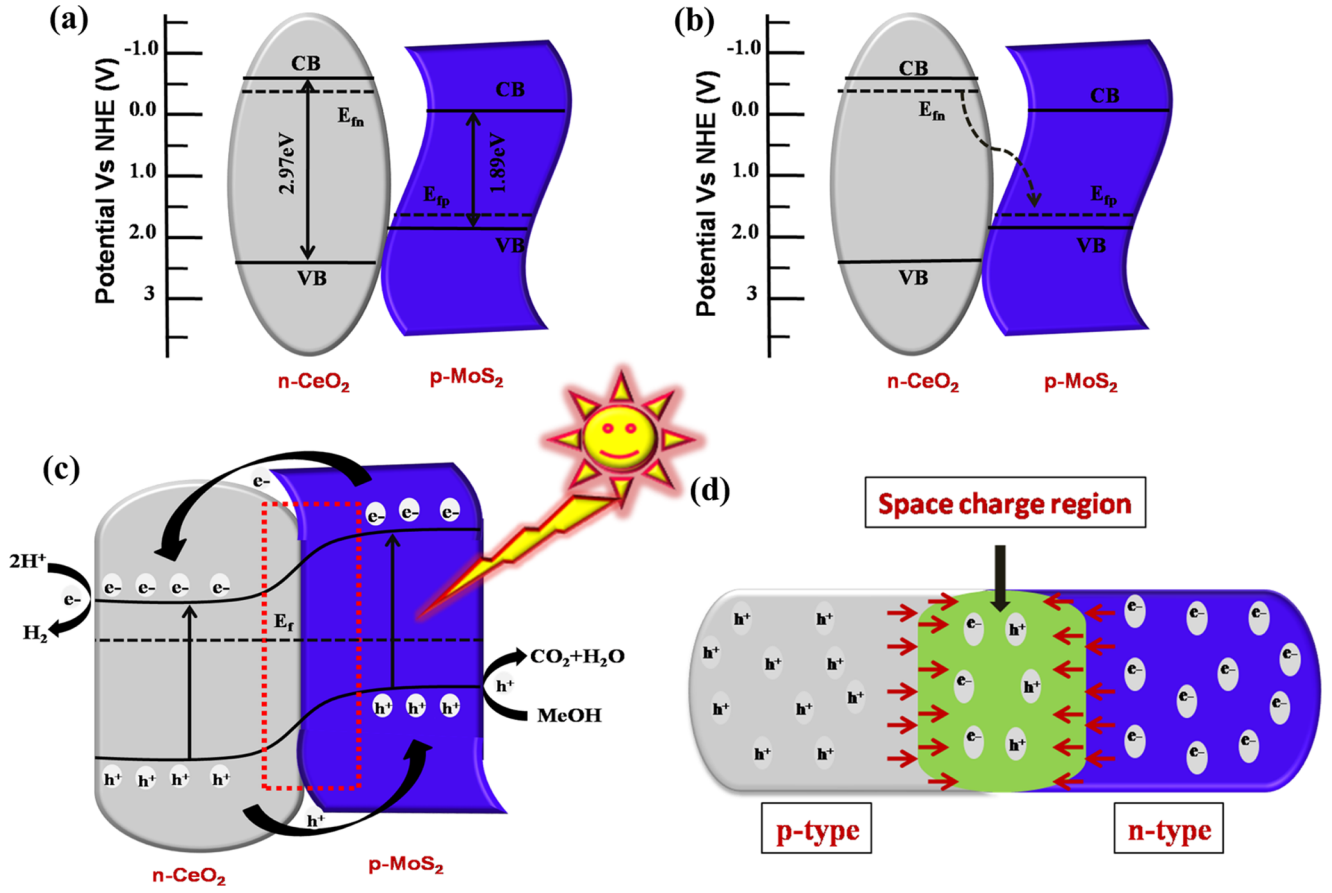

Figure 9. Schematic illustration of the proposed photocatalytic mechanistic pathway of charge separation and transfer in the 2% MoS_2/CeO_2 nanocomposite for solar light H_2 evolution. The energy band structure of p-MoS_2 and n-CeO_2 before coupling (a), the field direction of migration of electrons after made contact between p-MoS_2 and n-CeO_2 (b), the typical photoexcited charge transfer process at the thermodynamic equilibrium of the p−n heterojunction under visible light irradiation (c), and the internal electric field direction from n-type to p-type at the equilibrium (d).

efficient photocatalysts with potential applications in solar hydrogen generation.

EXPERIMENTAL SECTION

In this study, all of the chemicals were of analytical grade and were utilized without further purification. Double-distilled water was used in all experiments.

Synthesis of the Photocatalyst. *Preparation of CeO_2 Nanoparticles.* The CeO_2 nanoparticles were synthesized via a simple precipitation method. In a typical procedure, a mixture of an aqueous solution of cerium nitrate hexahydrate (2.1713 g), hexamethylenetetramine (HMT, 1.4162 g), and sodium dodecyl sulfate (SDS, 1.4564 g) was prepared in deionized water. A mixed solution containing 5 mL of HMT, 100 mL of deionized water, and 100 mL of the $Ce(NO_3)_3{\cdot}6H_2O$ solution was taken in a round bottom flask and heated up to 80 °C for 6 h. Then, 50 mL of SDS was added to the aforementioned solution and further heated up to 2 h. After the completion of the reaction, the precipitates were centrifuged and washed with distilled water followed by ethanol several times. The resulting white powder was dried under vacuum at room temperature (RT).[18]

Preparation of the MoS_2/CeO_2 Heterojunction Photocatalyst. The 2D MoS_2/CeO_2 heterojunction photocatalysts were successfully fabricated by a one-step in situ hydrothermal reaction of the as-harvested ceria nanoparticle powders with an aqueous solution containing sodium molybdate dihydrate and thiourea. The various weight percentage ratios of MoS_2 to CeO_2 were 0.5, 1, 2, 3, and 5. In a typical synthesis process, 0.5 g of the above prepared CeO_2 was dispersed in 60 mL of aqueous solution consisting of 1 mmol (0.007 g) $Na_2MoO_4{\cdot}2H_2O$ and 5 mmol (0.011 g) thiourea under ultrasonication for about 30 min. Next, the resulting homogeneous mixture suspension was transferred into a 100 mL Teflon-lined stainless steel autoclave and held at 210 °C for 24 h in an electric oven. After naturally cooled down to RT, the resultant precipitates were separated via centrifugation and thoroughly washed three times with distilled water followed by ethanol and dried in an oven at 80 °C for 12 h to obtain the x wt % 2D MoS_2/CeO_2 photocatalyst composite (where x = 0.5, 1, 2, 3, 5). In addition, MoS_2 was prepared by adopting the same reaction conditions in the absence of CeO_2.

Material Characterization. XRD characterization was done with Cu Kα radiation (λ = 0.15418 nm) at a scan rate of 0.05° min^{-1} from 10 to 80° following 40 kV of accelerating voltage and 30 mA of applied current. The UV−vis diffuse reflectance spectrum was obtained using a JASCO V-750 spectrophotometer in the wavelength range of 200−800 nm, and $BaSO_4$ was used as a standard reference material. By using a JASCO FP-8300 spectrofluorometer, the PL properties were evaluated, with an excitation wavelength of 340 nm. XPS characterization was done using a system consisting of a charge neutralizer and an Al Kα X-ray monochromatization source. TEM images were acquired and elemental mapping was

DOI: 10.1021/acsomega.7b00492
ACS Omega 2017, 2, 3745−3753

performed on a Philips TECNAI G^2 electron microscope operated at an accelerating voltage of 200 kV. All photoelectrochemical studies were carried out on IVIUMnSTAT, and the working electrode was prepared through an electrophoretic deposition technique using FTO as the conducting substrate. The respective counter and reference electrodes taken were Pt and Ag/AgCl. A 300 W Xe lamp was used as the light source. The Nyquist plot was acquired at 10^5−100 Hz at a zero bias in 0.1 M Na_2SO_4. The Mott−Schottky measurement was made at 500 Hz under dark conditions in 0.5 M H_2SO_4, whereas LSV plots were evaluated by sweeping the potential from 0 to −1.5 in a 0.1 M NaOH solution as the electrolyte.

Photocatalytic Water-Splitting Setup. The total reaction setup was mainly carried out in a 100 mL sealed quartz batch reactor round bottom flask and the 150 W xenon arc lamp (>400 nm) as the irradiated source followed by 1 M $NaNO_2$ as the UV cutoff filter was positioned 20 cm away from the aqueous suspension. The photocatalytic water-splitting mechanism was examined by dispersing 20 mg of the as-synthesized powdered catalyst into 20 mL of the aqueous solution of methanol with constant stirring to maintain the uniformity of the suspension throughout the reaction. Prior to light irradiation, N_2 gas was evacuated for 30 min through the reactor for complete removal of all dissolved oxygen. The amount of hydrogen gas evolved can be thoroughly measured by collecting the gas via the downward displacement of water and analyzed by gas chromatography.

■ ASSOCIATED CONTENT

Supporting Information

The Supporting Information is available free of charge on the ACS Publications website at DOI: 10.1021/acsomega.7b00492.

Individual band gap potential of neat CeO_2 and MoS_2, EDX spectra of the 2% MoS_2/CeO_2 nanocomposite, and the Mott−Schottky plot of neat CeO_2 and MoS_2 (Figures S1−S3) (PDF)

■ AUTHOR INFORMATION

Corresponding Author

*E-mail: kulamaniparida@soauniversity.ac.in.

ORCID

Kulamani Parida: 0000-0001-7807-5561

Notes

The authors declare no competing financial interest.

■ ACKNOWLEDGMENTS

The authors are highly thankful to the SOA university management for its cooperation and also to the American Chemical Society for funding through ACS Authors Rewards.

■ REFERENCES

(1) (a) Naik, B.; Kim, S. M.; Jung, C. H.; Moon, S. Y.; Kim, S. H.; Park, J. Y. Enhanced H_2 Generation of Au-Loaded, Nitrogen-Doped TiO_2 Hierarchical Nanostructures under Visible Light. *Adv. Mater. Interfaces* **2014**, *1*, No. 1300018. (b) Zhou, W.; Yin, Z.; Du, Y.; Huang, X.; Zeng, Z.; Fan, Z.; Liu, H.; Wang, J.; Zhang, H. Synthesis of few-layer MoS_2 nanosheet-coated TiO_2 nanobelt heterostructures for enhanced photocatalytic activities. *Small* **2013**, *9*, 140−147. (c) Parida, K. M.; Naik, B. Synthesis of mesoporous TiO_{2-x} N_x spheres by template free homogeneous co-precipitation method and their photocatalytic activity under visible light illumination. *J. Colloid Interface Sci.* **2009**, 333, 269−276. (d) Park, J. Y.; Kim, S. M.; Lee, H.; Naik, B. Hot Electron and Surface Plasmon-Driven Catalytic Reaction in Metal−Semiconductor Nanostructures. *Catal. Lett.* **2014**, *144*, 1996−2004. (e) Yu, C.; Zhou, W.; Zhu, L.; Li, G.; Yang, K.; Jin, R. Integrating plasmonic Au nanorods with dendritic like α-$Bi_2O_3/Bi_2O_2CO_3$ heterostructures for superior visible-light-driven photocatalysis. *Appl. Catal., B: Environ.* **2016**, *184*, 1−11.

(2) (a) Pany, S.; Naik, B.; Martha, S.; Parida, K. Plasmon induced nano Au particle decorated over S, N-Modified TiO_2 for exceptional photocatalytic hydrogen evolution under visible light. *ACS Appl. Mater. Interfaces* **2014**, *6*, 839−846. (b) Naik, B.; Parida, K.; Gopinath, C. S. Facile synthesis of N-and S-incorporated nanocrystalline TiO_2 and direct solar-light-driven photocatalytic activity. *J. Phys. Chem. C* **2010**, *114*, 19473−19482. (c) Zhu, Y.; Ling, Q.; Liu, Y.; Wang, H.; Zhu, Y. Photocatalytic H_2 evolution on MoS_2−TiO_2 catalysts synthesized via mechanochemistry. *Phys. Chem. Chem. Phys.* **2015**, *17*, 933−940. (d) Martha, S.; Sahoo, P. C.; Parida, K. An overview on visible light responsive metal oxide based photocatalysts for hydrogen energy production. *RSC Adv.* **2015**, *5*, 61535−61553. (e) Kuang, P.-Y.; Su, Y.-Z.; Xiao, K.; Liu, Z.-Q.; Li, N.; Wang, H.-J.; Zhang, J. Double-Shelled CdS- and CdSe-Cosensitized ZnO Porous Nanotube Arrays for Superior Photoelectrocatalytic Applications. *ACS Appl. Mater. Interfaces* **2015**, *7*, 16387−16394. (f) Kuang, P.-Y.; Ran, J.-R.; Liu, Z.-Q.; Wang, H.-J.; Li, N.; Su, Y.-Z.; Jin, Y.-G.; Qiao, S.-Z. Enhanced Photoelectrocatalytic Activity of BiOI Nanoplate−Zinc Oxide Nanorod p−n Heterojunction. *Chem. − Eur. J.* **2015**, *21*, 15360−15368.

(3) (a) Zhang, X.; Zhang, N.; Xu, Y.-J.; Tang, Z.-R. One-dimensional CdS nanowires−CeO_2 nanoparticles composites with boosted photocatalytic activity. *New J. Chem.* **2015**, *39*, 6756−6764. (b) Wei, R.-B.; Kuang, P.-Y.; Cheng, H.; Chen, Y.-B.; Long, J.-Y.; Zhang, M.-Y.; Liu, Z.-Q. Plasmon-Enhanced Photoelectrochemical Water Splitting on Gold Nanoparticle Decorated ZnO/CdS Nanotube Arrays. *ACS Sustainable Chem. Eng.* **2017**, *5*, 4249−4257. (c) Liu, Z.-Q.; Kuang, P.-Y.; Wei, R.-B.; Li, N.; Chen, Y.-B.; Su, Y.-Z. BiOBr nanoplate-wrapped ZnO nanorod arrays for high performance photoelectrocatalytic application. *RSC Adv.* **2016**, *6*, 16122−16130.

(4) You, D.; Pan, B.; Jiang, F.; Zhou, Y.; Su, W. CdS nanoparticles/CeO_2 nanorods composite with high-efficiency visible-light-driven photocatalytic activity. *Appl. Surf. Sci.* **2016**, *363*, 154−160.

(5) (a) Manwar, N. R.; Chilkalwar, A. A.; Nanda, K. K.; Chaudhary, Y. S.; Subrt, J.; Rayalu, S. S.; Labhsetwar, N. K. Ceria supported Pt/PtO-nanostructures: Efficient photocatalyst for sacrificial donor assisted hydrogen generation under Visible-NIR light irradiation. *ACS Sustainable Chem. Eng.* **2016**, *4*, 2323−2332. (b) Yang, J.; Wang, D.; Han, H.; Li, C. Roles of Cocatalysts in Photocatalysis and Photoelectrocatalysis. *Acc. Chem. Res.* **2013**, *46*, 1900−1909.

(6) (a) Xia, J.; Ge, Y.; Zhao, D.; Di, J.; Ji, M.; Yin, S.; Li, H.; Chen, R. Microwave-assisted synthesis of few-layered MoS_2/BiOBr hollow microspheres with superior visible-light-response photocatalytic activity for ciprofloxacin removal. *CrystEngComm* **2015**, *17*, 3645−3651. (b) Song, Y.; Lei, Y.; Xu, H.; Wang, C.; Yan, J.; Zhao, H.; Xu, Y.; Xia, J.; Yin, S.; Li, H. Synthesis of few-layer MoS_2 nanosheet-loaded Ag_3PO_4 for enhanced photocatalytic activity. *Dalton Trans.* **2015**, *44*, 3057−3066. (c) Lin, T.; Wang, J.; Guo, L.; Fu, F. Fe_3O_4@ MoS_2 core−shell composites: preparation, characterization, and catalytic application. *J. Phys. Chem. C* **2015**, *119*, 13658−13664.

(7) (a) Chang, K.; Mei, Z.; Wang, T.; Kang, Q.; Ouyang, S.; Ye, J. MoS_2/graphene cocatalyst for efficient photocatalytic H_2 evolution under visible light irradiation. *ACS Nano* **2014**, *8*, 7078−7087. (b) Balendhran, S.; Ou, J. Z.; Bhaskaran, M.; Sriram, S.; Ippolito, S.; Vasic, Z.; Kats, E.; Bhargava, S.; Zhuiykov, S.; Kalantar-Zadeh, K. Atomically thin layers of MoS_2 via a two step thermal evaporation−exfoliation method. *Nanoscale* **2012**, *4*, 461−466.

(8) (a) Ye, G.; Gong, Y.; Lin, J.; Li, B.; He, Y.; Pantelides, S. T.; Zhou, W.; Vajtai, R.; Ajayan, P. M. Defects engineered monolayer MoS_2 for improved hydrogen evolution reaction. *Nano Lett.* **2016**, *16*, 1097−1103. (b) Zhou, X.; Lickleder, M.; Schmuki, P. Thin MoS_2 on TiO_2 nanotube layers: An efficient co-catalyst/harvesting system for photocatalytic H_2 evolution. *Electrochem. Commun.* **2016**, *73*, 33−37. (c) Yuan, Y.-J.; Tu, J.-R.; Ye, Z.-J.; Chen, D.-Q.; Hu, B.; Huang, Y.-W.;

DOI: 10.1021/acsomega.7b00492
ACS Omega 2017, 2, 3745−3753

Chen, T.-T.; Cao, D.-P.; Yu, Z.-T.; Zou, Z.-G. MoS_2-graphene/$ZnIn_2S_4$ hierarchical microarchitectures with an electron transport bridge between light-harvesting semiconductor and cocatalyst: A highly efficient photocatalyst for solar hydrogen generation. *Appl. Catal. B: Environ.* **2016**, *188*, 13−22. (d) Yuan, Y.-J.; Chen, D.-Q.; Huang, Y.-W.; Yu, Z.-T.; Zhong, J.-S.; Chen, T.-T.; Tu, W.-G.; Guan, Z.-J.; Cao, D.-P.; Zou, Z.-G. MoS_2 Nanosheet-Modified $CuInS_2$ Photocatalyst for Visible-Light-Driven Hydrogen Production from Water. *ChemSusChem* **2016**, *9*, 1003−1009. (e) Zong, X.; Yan, H.; Wu, G.; Ma, G.; Wen, F.; Wang, L.; Li, C. Enhancement of Photocatalytic H_2 Evolution on CdS by Loading MoS_2 as Cocatalyst under Visible Light Irradiation. *J. Am. Chem. Soc.* **2008**, *130*, 7176−7177.

(9) (a) Yuan, Y.-J.; Ye, Z.-J.; Lu, H.-W.; Hu, B.; Li, Y.-H.; Chen, D.-Q.; Zhong, J.-S.; Yu, Z.-T.; Zou, Z.-G. Constructing anatase TiO_2 nanosheets with exposed (001) facets/layered MoS_2 two-dimensional nanojunctions for enhanced solar hydrogen generation. *ACS Catal.* **2016**, *6*, 532−541. (b) Kong, Z.; Yuan, Y.-J.; Chen, D.; Fang, G.; Yang, Y.; Yang, S.; Cao, D. Noble-metal-free MoS_2 nanosheets modified-InVO4 heterostructures for enhanced visible-light-driven photocatalytic H_2 production. *Dalton Trans.* **2017**, *46*, 2072−2076.

(10) (a) Wang, W.; Huang, X.; Wu, S.; Zhou, Y.; Wang, L.; Shi, H.; Liang, Y.; Zou, B. Preparation of p−n junction $Cu_2O/BiVO_4$ heterogeneous nanostructures with enhanced visible-light photocatalytic activity. *Appl. Catal. B: Environ.* **2013**, *134*−*135*, 293−301. (b) Zhao, W.; Liu, Y.; Wei, Z.; Yang, S.; He, H.; Sun, C. Fabrication of a novel p−n heterojunction photocatalyst n-$BiVO_4$@ p-MoS_2 with core−shell structure and its excellent visible-light photocatalytic reduction and oxidation activities. *Appl. Catal. B: Environ.* **2016**, *185*, 242−252. (c) Yu, C.; Wei, L.; Zhou, W.; Dionysiou, D. D.; Zhu, L.; Shu, Q.; Liu, H. A visible-light-driven core-shell like Ag_2S@Ag_2CO_3 composite photocatalyst with high performance in pollutants degradation. *Chemosphere* **2016**, *157*, 250−261.

(11) Li, H.; Yu, K.; Lei, X.; Guo, B.; Fu, H.; Zhu, Z. Hydrothermal Synthesis of Novel $MoS_2/BiVO_4$ Hetero-Nanoflowers with Enhanced Photocatalytic Activity and a Mechanism Investigation. *J. Phys. Chem. C* **2015**, *119*, 22681−22689.

(12) Pareek, A.; Kim, H. G.; Paik, P.; Borse, P. H. Ultrathin MoS_2−MoO_3 nanosheets functionalized CdS photoanodes for effective charge transfer in photoelectrochemical (PEC) cells. *J. Mater. Chem. A* **2017**, *5*, 1541−1547.

(13) Liu, Y.; Yu, Y.-X.; Zhang, W.-D. MoS_2/CdS heterojunction with high photoelectrochemical activity for H_2 evolution under visible light: the role of MoS_2. *J. Phys. Chem. C* **2013**, *117*, 12949−12957.

(14) Zhang, K.; Kim, W.; Ma, M.; Shi, X.; Park, J. H. Tuning the charge transfer route by p-n junction catalysts embedded with CdS nanorods for simultaneous efficient hydrogen and oxygen evolution. *J. Mater. Chem. A* **2015**, *3*, 4803−4810.

(15) Gong, X.; Gu, Y.-Q.; Li, N.; Zhao, H.; Jia, C.-J.; Du, Y. Thermally stable hierarchical nanostructures of ultrathin MoS_2 nanosheet-coated CeO_2 hollow spheres as catalyst for ammonia decomposition. *Inorg. Chem.* **2016**, *55*, 3992−3999.

(16) Li, N.; Zhao, H.; Zhang, Y.; Liu, Z.; Gong, X.; Du, Y. Core−shell structured CeO_2@MoS_2 nanocomposites for high performance symmetric supercapacitors. *CrystEngComm* **2016**, *18*, 4158−4164.

(17) Li, X.; Zhang, Z.; Yao, C.; Lu, X.; Zhao, X.; Ni, C. Attapulgite-CeO_2/MoS_2 ternary nanocomposite for photocatalytic oxidative desulfurization. *Appl. Surf. Sci.* **2016**, *364*, 589−596.

(18) Taniguchi, T.; Sonoda, Y.; Echikawa, M.; Watanabe, Y.; Hatakeyama, K.; Ida, S.; Koinuma, M.; Matsumoto, Y. Intense photoluminescence from ceria-based nanoscale lamellar hybrid. *ACS Appl. Mater. Interfaces* **2012**, *4*, 1010−1015.

(19) Min, S.; Lu, G. Sites for high efficient photocatalytic hydrogen evolution on a limited-layered MoS_2 cocatalyst confined on graphene sheets——the role of graphene. *J. Phys. Chem. C* **2012**, *116*, 25415−25424.

(20) Mani, A. D.; Nandy, S.; Subrahmanyam, C. Synthesis of CdS/CeO_2 nanomaterials for photocatalytic H_2 production and simultaneous removal of phenol and Cr (VI). *J. Environ. Chem. Eng.* **2015**, *3*, 2350−2357.

(21) Vattikuti, S. V. P.; Byon, C.; Reddy, C. V.; Ravikumar, R. Improved photocatalytic activity of MoS_2 nanosheets decorated with SnO_2 nanoparticles. *RSC Adv.* **2015**, *5*, 86675−86684.

(22) (a) Islam, M. J.; Reddy, D. A.; Choi, J.; Kim, T. K. Surface oxygen vacancy assisted electron transfer and shuttling for enhanced photocatalytic activity of a Z-scheme CeO_2−AgI nanocomposite. *RSC Adv.* **2016**, *6*, 19341−19350. (b) Rajendran, S.; Khan, M. M.; Gracia, F.; Qin, J.; Gupta, V. K.; Arumainathan, S. Ce^{3+}ion-induced visible-light photocatalytic degradation and electrochemical activity of ZnO/CeO_2 nanocomposite. *Sci. Rep.* **2016**, *6*, No. 31641.

(23) Mansingh, S.; Padhi, D.; Parida, K. Enhanced photocatalytic activity of nanostructured Fe doped CeO_2 for hydrogen production under visible light irradiation. *Int. J. Hydrogen Energy* **2016**, *41*, 14133−14146.

(24) Zhang, X.; Zhang, L.; Xie, T.; Wang, D. Low-temperature synthesis and high visible-light-induced photocatalytic activity of BiOI/TiO_2 heterostructures. *J. Phys. Chem. C* **2009**, *113*, 7371−7378.

(25) Ge, L.; Han, C.; Xiao, X.; Guo, L. Synthesis and characterization of composite visible light active photocatalysts MoS_2−gC_3N_4 with enhanced hydrogen evolution activity. *Int. J. Hydrogen Energy* **2013**, *38*, 6960−6969.

(26) Nayak, S.; Mohapatra, L.; Parida, K. Visible light-driven novel g-C_3N_4/NiFe-LDH composite photocatalyst with enhanced photocatalytic activity towards water oxidation and reduction reaction. *J. Mater. Chem. A* **2015**, *3*, 18622−18635.

(27) Xu, Z.; Lin, Y.; Yin, M.; Zhang, H.; Cheng, C.; Lu, L.; Xue, X.; Fan, H. J.; Chen, X.; Li, D. Understanding the Enhancement Mechanisms of Surface Plasmon-Mediated Photoelectrochemical Electrodes: A Case Study on Au Nanoparticle Decorated TiO_2 Nanotubes. *Adv. Mater. Interfaces* **2015**, *2*, No. 1500169.

(28) Zhao, Y.-F.; Yang, Z.-Y.; Zhang, Y.-X.; Jing, L.; Guo, X.; Ke, Z.; Hu, P.; Wang, G.; Yan, Y.-M.; Sun, K.-N. Cu_2O decorated with cocatalyst MoS_2 for solar hydrogen production with enhanced efficiency under visible light. *J. Phys. Chem. C* **2014**, *118*, 14238−14245.

(29) Yue, X.; Yi, S.; Wang, R.; Zhang, Z.; Qiu, S. A novel and highly efficient earth-abundant Cu_3P with TiO_2 "P−N" heterojunction nanophotocatalyst for hydrogen evolution from water. *Nanoscale* **2016**, *8*, 17516−17523.

DOI: 10.1021/acsomega.7b00492
ACS Omega 2017, 2, 3745−3753